

Oxidation Mechanism of C in MgO–C Refractory Bricks

S. K. Sadrnezhad,[†] S. Mahshid, B. Hashemi, and Z. A. Nemati

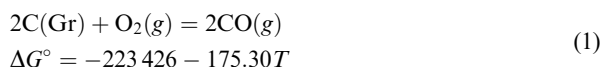
Department of Materials Science and Engineering, Center of Excellence for Advanced Processes of Production of Materials, Sharif University of Technology, Tehran 11365-9466, Iran

Kinetics of oxidation of MgO–C refractory bricks containing 14.3% graphite, 80.9% magnesia, and 4.8% phenolic resin is investigated comprehensively. Effect of temperature and grain size distribution on the rate of oxidation of graphite is evaluated by application of a mathematical model developed on the basis of shrinking core/progressive conversion regime to the gas–solid processes involved. Incorporation of the experimental data into the mathematical model indicates that a mixed controlling mechanism governs the oxidation rate. Three activation energies were recognized: (a) 68 kJ/mol for chemical adsorption of gas on the surface of the graphite flakes, (b) 22 kJ/mol for pore diffusion of the gases within the decarburized layer, and (c) 140 kJ/mol for internal diffusion of the reactants toward the active reaction sites. The first process was influential at all temperatures, the second was confined to the temperatures above 800°C and the third was attributed to the temperatures lower than 800°C. Empirical data indicated a much lower weight loss rate at temperatures lower than 800°C.

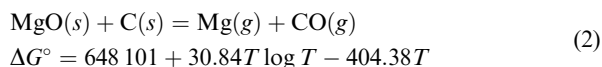
I. Introduction

PRESENCE of graphite in MgO–C refractory bricks results in high slag corrosion resistance, thermal shock endurance, wettability reduction, and diminished thermal expansion.^{1,2} Undesirable property change is, therefore, expected to take place when embedded graphite oxidizes via a direct or an indirect carbon oxygen combustion reaction³:

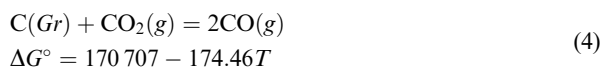
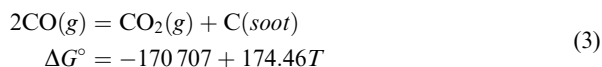
(1) *Direct oxidation of graphite with oxygen:*



(2) *Indirect oxidation of graphite with MgO particles:*



(3) *Boudouard dissociation of CO accompanied with graphite oxidation:*



At temperatures lower than 1400°C, reactions (1) and (4) are the main oxidation stages. At temperatures greater than 1400°C, reaction (2) becomes important. This solid–solid reduction reaction produces a considerable magnesium vapor pressure at

higher temperatures. Subsequent magnesium condensation results in formation of a dense MgO layer.⁴ This layer increases the refractory resistance to the subsequent oxidation reaction.^{5,6}

Direct or indirect oxidation both have crucial effects on the refractory degradation.^{4–6} Reaction (4) is endothermic and is favored by higher temperatures.³ Exothermic reaction (1) causes increasing of the temperature at the surface of the graphite flakes. Progress of reaction (3) at areas close to graphite flakes causes higher CO₂ partial pressure and formation of more CO according to reaction (4).

Steelmaking furnaces with oxidizing atmosphere cause graphite oxidation especially during lancing, tapping, or preparation.^{7–9} A number of publications address the role of MgO particle size and the amount of graphite on physico-chemical properties of MgO–C refractories.^{10–12} A number of authors have previously studied the oxidation kinetics of MgO–C refractories.^{13–17} Li *et al.*¹³ have used the atmospheric analysis of the gases surrounding the oxidizing sample. Ghosh *et al.*¹⁴ and Faghihi-Sani and Yamauchi¹⁵ have used the weight-loss measurements for oxidation reactions. These studies have, however, been confined to temperatures above 800°C. Single-step kinetic control has also usually been considered to simplify the influential kinetic parameter evaluations.^{13–15}

Low-temperature oxidation kinetics is almost totally unknown. Such temperatures are, however, important because of the following two requirements: (a) grasping a comprehensive understanding of the mechanisms for the MgO–C oxidation process and (b) inevitable occasional uses of the materials from ambient to the higher temperatures. This paper reports on the best-fitting mechanisms for oxidation reactions occurring at 600°–1250°C working temperatures.¹⁸ Samples with different Andreassen distribution coefficients were oxidized and fractional weight losses were measured. The experimental data were compared with the simulation results. Diffusion coefficients, rate constants, and activation energies of the influencing steps were graphically determined.

II. Experimental Procedure

Chinese sintered magnesia grains with chemical composition and density illustrated in Table I and size distribution given in Table II and Chinese graphite flakes containing 5 wt% ash with composition indicated in Table III were used to produce cylindrical refractory probes required for oxidation tests. The probes had a diameter of 30 mm and a height of 25 mm. They contained 14.3 wt% graphite and 4.8 wt% liquid phenolic resin (Novalac Pars Resin, Isfahan, Iran) used as a binder. The probes were diepressed unidirectionally and tempered at 240°C for 18 h. Their density and apparent porosities were evaluated by 24 h crude oil soaking. They were heated again at 600°C for 5 h in a coke bed to remove their volatile species. Density and apparent porosity measurements were repeated again according to the same procedure, and the mean values obtained were recorded for the model calculations.

Isothermal oxidation tests were carried out at 600°, 650°, 700°, 800°, 950°, 1100°, and 1250°C. A tubular furnace (Fig. 1) allowing natural convection of the air was used for this purpose. Each probe was placed on an alumina tube. The tube was grad-

M. Rigaud—contributing editor

Manuscript No. 20825. Received July 31, 2005; approved October 31, 2005.

[†]Author to whom correspondence should be addressed. e-mail: sadrnezh@sharif.edu

Table I. Mean Chemical Analysis and Density of the Chinese Sintered Magnesia Grains used in this Research

Composition	MgO	CaO	SiO ₂	Al ₂ O ₃	Fe ₂ O ₃	L.O.I
Weight percent	97.1	1.26	0.56	0.09	0.89	0.01
Density (g/cm ³)						3.51

ually raised up in order to insert the probe into the furnace. This took 2–3 min. The weight losses corresponding to this stage were neglected. For unidirectional oxidation from the periphery toward the centerline of a probe, its top and bottom sides were covered by two pieces of alumina plates. Axial diffusion of oxygen was thus prevented from the top or bottom into the probe. The weight changes of the refractory materials were measured against time. The fractional weight loss (X) was calculated based on the following definition:

$$\text{Fractional weight loss} \\ = X = \frac{\text{Weight loss at time } t}{\text{Total weight loss after complete oxidation}}$$

Total weight loss was experimentally determined by measurement of the weight change when all the C content of the probe was burned at 1000°C. The results showed 2%–4% difference with the calculated total carbon contents. They were therefore assumed the same as the theoretical figures.

Each cylindrical probe was partially powdered when it was sectioned with a rotational cutter. The powder was used for XRD analysis of the MgO–C. CuK α radiation ($\lambda = 1.54 \text{ \AA}$) produced by a 40 kV Philips PW-1730 diffractometer (Philips, the Netherlands) was used for sample characterization.

III. Modeling

Appropriate models were chosen through observation of the cross-sectional areas of the probes (Fig. 2). No dimensional changes were observed because of the oxidation. After oxidation, the cross-section of the probes showed both oxidized and non-oxidized regions. At low temperatures, no recognizable boundary was observed (Figs. 2(b) and (c)). At higher temperatures, a sharp boundary emerged (Figs. 2(f)–(h)). A change in the oxidation mechanism was, therefore, expected around 800°C. Progressive conversion was attributed to the lower temperatures, while the shrinking core model was more appropriate for the higher temperatures.

Existence of a sharp boundary at temperatures higher than 800°C indicated a considerable chemical reaction rate as compared with the inter-diffusion of the gases within the porous decarburized layer of the specimens. Because of high reactivity of the oxygen with carbon atoms at these temperatures—no matter where they come from (phenolic resin or graphite flakes)—the reaction front advanced distinguishably toward

Table II. Size Distribution of MgO Grains with Different Andreason Coefficients, n_A

Raw materials	Grain size (mm)	wt%		
		$n_A = 0.3$	$n_A = 0.5$	$n_A = 0.7$
Sintered MgO	3–5	11.49	18.22	24.27
	2–3	7.93	11.48	13.99
	1–2	11.57	14.97	16.43
	0.1–1	24.92	24.81	20.95
	< 0.1	24.99	11.42	5.26
Total MgO	Mixed as above	80.9		
Graphite flake	Fixed	14.3		
Phenolic resin	—	4.8		

Table III. Mean Chemical Analysis of the Ash Present in Graphite Flakes used in this Research

Composition	SiO ₂	Al ₂ O ₃	MgO	CaO	Na ₂ O	K ₂ O	Fe
Percentage	50.2	17.10	7.67	5.06	0.79	1.37	17.8

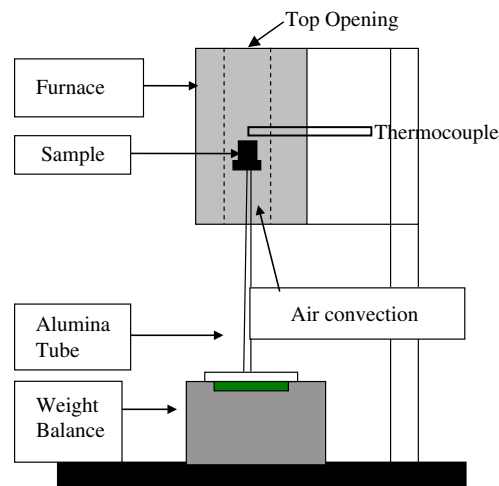
the center of the specimen. Isothermal shrinking core models developed for constant size specimens were successfully applied to oxidation of the probes at these temperatures.^{18,19}

At temperatures lower than 800°C, soot is formed according to the Boudouard reaction (Eq. (3)).^{20,21} Soot is a carbonaceous material generated during combustion of carbon-based materials and is usually found as relatively dense spheres in the size range of 20–30 nm.^{22,23} The spheres consist of nearly concentric layers around a nucleus. The nucleus has an arrangement similar to that of graphite. The particles grow in chain-like aggregates.²⁴ As reaction (4) is endothermic,³ its preferential site is the surface of the graphite flakes that is hot because of the occurrence of the oxidation reactions. Slightly cooler locations like porosity opening ends (see Fig. 3) are suitable places for soot formation according to reaction (3), which is also exothermic. Any oxygen molecule that reaches the surface of a graphite flake results in a slight temperature raise. This raise causes the formation of more CO according to the endothermic reaction (4). Circulation of the entrapped CO₂ within the empty space around the graphite flake results in enhancement of CO₂ partial pressure that induces the formation of more CO according to reaction (4).

Precipitation of cloudy soot aggregates within open-hole terminals and local pore walls surrounding graphite flakes causes pore-end blockage (Fig. 3). The inwards transfer of O₂ to the graphite flakes as well as the outwards migration of CO/CO₂ gases away from the graphite surfaces according to the pore diffusion mechanism become hence impossible. Pore inter-diffusion of O₂/N₂/CO/CO₂ gases will then cease from the close-ended pores physically separated from graphite flakes. Because of very small end surfaces available to the O₂/soot reactions, the rate of soot oxidation is not so significant as to affect the total oxidation rate. An internal diffusion mechanism will thus become important in the oxidation rate of the probes.

Pyrolysis of phenolic resin can also produce polymer coke. The product is micro-porous, with pore dimensions of molecular size.²⁵ The lattice of this coke has a ribbon-like structure. Several ribbons may be stacked up to plate-like polymer/glassy carbon structure.²³ Resin-based carbon is better in filling the spaces between the MgO grains.^{25,26}

Below 800°C, the rate of oxidation of the probes becomes so small that the sharp reaction fronts seen at $T \geq 800^\circ\text{C}$ substitute with indistinguishable progressive reaction fronts observable in Fig. 2. A progressive conversion model with a mixed control

**Fig. 1. Schematic representation of the setup used for oxidation weight-loss measurements.**

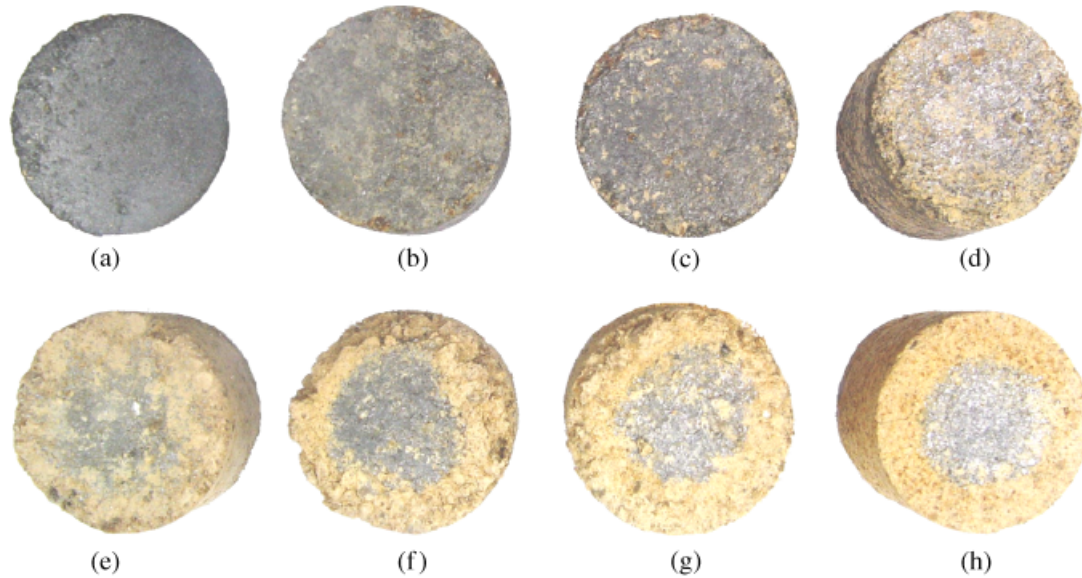


Fig. 2. Photographs of MgO–C refractory samples: (a) before oxidation, (b) oxidized at 600°C, (c) oxidized at 650°C, (d) oxidized at 700°C, (e) oxidized at 800°C, (f) oxidized at 950°C, (g) oxidized at 1100°C, and (h) oxidized at 1250°C.

regime gives the best explanation of the data obtained at these temperatures.

The following potential steps are considered to influence the rate of the oxidation reaction:

(a) Mass transfer from atmosphere to the surface of the probe (ED).

(b) Inter-diffusion of the gases within the decarburized layer of the probe toward the active reaction sites (PD).

(c) Internal diffusion of the oxidizing and the produced gases through magnesia grains surrounding the graphite flakes (ID).

(d) Chemical adsorption (CA) of the reacting gas at the surface of the graphite flakes (CA).

The conversion time (the time elapsed after the start of oxidation) is hence correlated with the following four functions: f_{ED} , f_{PD} , f_{ID} , and f_{CA} .¹⁹

$$t = \tau_{ED}f_{ED}(X) + \tau_{PD}f_{PD}(X) + \tau_{ID}f_{ID}(X) + \tau_{CA}f_{CA}(X) \quad (5)$$

τ_{ED} , τ_{PD} , τ_{ID} , and τ_{CA} are the total conversion times corresponding to the specified rate controlling steps¹⁸:

$$f_{ED}(X) = X \quad (6)$$

$$f_{PD}(X) = X + (1 - X) \times \ln(1 - X) \quad (7)$$

$$f_{ID}(X) = X^2 \quad (8)$$

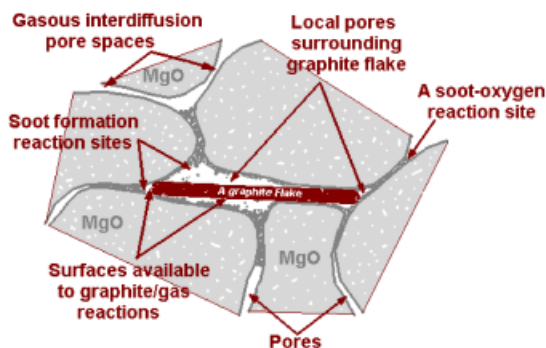


Fig. 3. Blockage of the pore terminals in MgO–C refractory bricks by soot precipitation at temperatures lower than 800°C.

$$f_{CA}(X) = X \quad (9)$$

Equations (6) and (7) are related to the sharp front cylindrical geometry,¹⁹ while Equations (8) and (9) correspond to a flat graphite flake.²⁷ The radius of the unreacted core, r_c , is related to the fractional conversion, X , of the shrinking core probes revealing a sharp reaction front²⁷:

$$X = 1 - (r_c/R)^2 \quad (10)$$

R is the initial radius of the MgO–C probe. For the progressive conversion regime with indistinguishable reaction front, the mean half-thickness, δ , of the flakes is proportionally related to the fractional conversion, X :

$$X = 1 - \delta/L \quad (11)$$

L is the initial mean half-thickness of the graphite flakes. The fractional conversion of the refractory material is on the other hand related to the weight loss of the sample.

Applying the experimental data into the mathematical correlations 5–9, one can obtain the total conversion time of the sample. Best-fit results are obtainable through the application of various mathematical procedures.^{16,19} From the experimental data, each $\tau_i f_i(X)$ term can be evaluated by minimizing the least mean square difference of the experimental with the theoretical figures. Results might then be plotted against progressing time of the reaction. In case a linear diagram is obtained, a one-step controlling mechanism can be considered to prevail. This usually associates with a total conversion time τ_i determined from slopes of the linear curves.

Chances exist that double or multiple stage mechanisms give a better fit of the data with the model equation. The least mean square technique can appropriately provide such fitting conditions. The deviation of the experimental results from the calculated ones is thus evaluated from

$$\sigma^2 = \sum_{i=1}^n [t_i - \tau_{PD}f_{PD}(X_i) - \tau_{ID}f_{ID}(X_i) - \tau_{CA}f_{CA}(X_i)]^2 \quad (12)$$

To minimize deviation, the derivative of σ^2 with respect to τ_{PD} , τ_{ID} , and τ_{CA} must be zero. That is

$$\frac{\partial \sigma^2}{\partial \tau_{PD}} = 0, \quad \frac{\partial \sigma^2}{\partial \tau_{ID}} = 0, \quad \frac{\partial \sigma^2}{\partial \tau_{CA}} = 0 \quad (13)$$

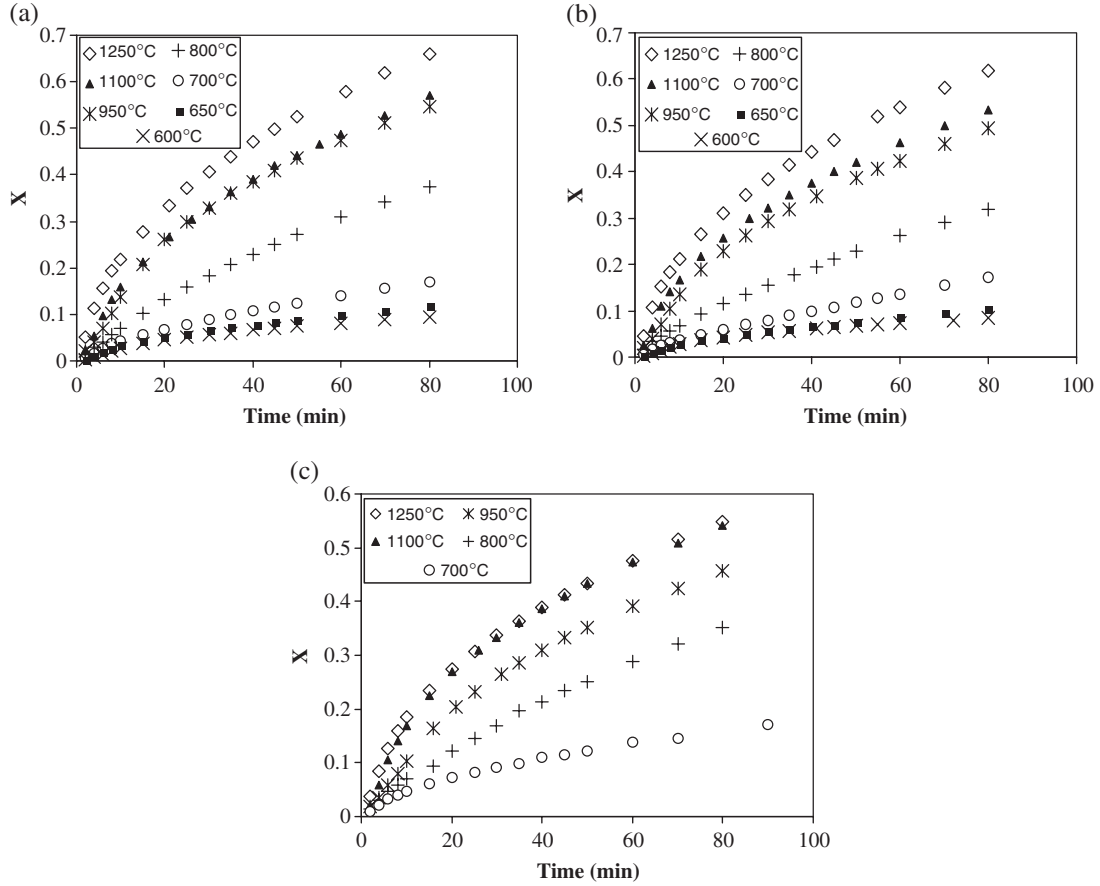


Fig. 4. Changes of the fractional weight loss with time for different Andraesen distribution numbers (a) $n_A = 0.3$, (b) $n_A = 0.5$ and (c) $n_A = 0.7$.

Combination of (12) with (13) yields

$$\begin{aligned} & \tau_{PD} \sum_{i=1}^n [f_{PD}(X_i)]^2 + \tau_{ID} \sum_{i=1}^n f_{PD}(X_i) f_{ID}(X_i) + \tau_{CA} \\ & \times \sum_{i=1}^n f_{PD}(X_i) f_{CA}(X_i) \\ & = \sum_{i=1}^n t_i f_{PD}(X_i) \end{aligned} \quad (14)$$

$$\begin{aligned} & \tau_{PD} \sum_{i=1}^n f_{PD}(X_i) f_{ID}(X_i) + \tau_{ID} \sum_{i=1}^n [f_{ID}(X_i)]^2 + \tau_{CA} \\ & \times \sum_{i=1}^n f_{ID}(X_i) f_{CA}(X_i) \\ & = \sum_{i=1}^n t_i f_{ID}(X_i) \end{aligned} \quad (15)$$

$$\begin{aligned} & \tau_{PD} \sum_{i=1}^n f_{PD}(X_i) f_{CA}(X_i) + \tau_{ID} \sum_{i=1}^n f_{ID}(X_i) f_{CA}(X_i) \\ & + \tau_{CA} \sum_{i=1}^n [f_{CA}(X_i)]^2 \\ & = \sum_{i=1}^n t_i f_{CA}(X_i) \end{aligned} \quad (16)$$

Solving the above equations will result in evaluation of τ_i . A comparison of the latter helps to determine the rate controlling step as well as the activation energies of the oxidation process. Similar techniques have been used to develop computer software to check the data obtained in this research.¹⁸ The software is developed in the Matlab 7.0 environment. It is modified for

mixed particle shape factors influential to a single progressing reaction. Prevalence of individual single steps proves imprecise for all empirically reported figures. Mixed controlling regimes are therefore tested and found to be appropriate with the present boundary conditions.

Fractional conversions obtained against time do not give a straight line in this research (Fig. 4). Double-function combinations give straight lines, however, when software calculated slopes are assigned to the modeling equations (Eq. (5)). The most promising results show a two-step controlling system for all temperatures and Andraesen distribution numbers used in this research.

The prevailing two-step mechanism could best be described by cross-sectional observations (Fig. 2) and XRD graphs of the oxidized MgO-C probes (Fig. 5). Total conversion times produced this way ought to be positive numbers. They must be larger than those evaluated for the non-prevailing mechanisms.^{19,27} Smaller deviation numbers and better correlation factors are two other important criteria explaining the goodness of a specified reaction mechanism.

IV. Results and Discussion

The total conversion time of each individual step is computable through utilization of the modeling software to the oxidation results shown in Fig. 4. Table IV summarizes the computed figures. The mean stoichiometric coefficient b of the reaction is estimated from the equilibrium CO/CO₂ ratio produced at different temperatures. It is defined as the number of C atoms required for reaction with one mole of O₂ at equilibrium



Two-step mechanisms have shown the best fit with lowest variance at all experimental conditions. An example is plotted in

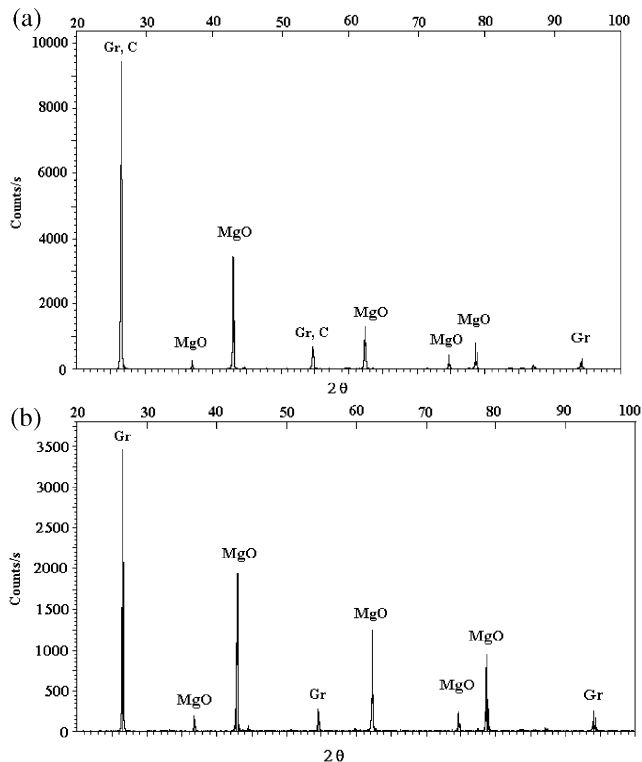


Fig. 5. X-ray diffraction graphs of the samples oxidized at (a) 600°C and (b) 1100°C. Gr refers to graphite and C refers to soot.

Fig. 6. The activation energies have been different for similar diffusion steps at different temperatures.

Kinetic parameters are obtained from the total conversion times of three different processes stated in Table IV. The individual total conversion times, pore diffusion coefficients, internal diffusion coefficients, and the CA rate constants of the oxidation reactions are summarized in the table. As can be seen from the table, the values of three kinetic parameters are

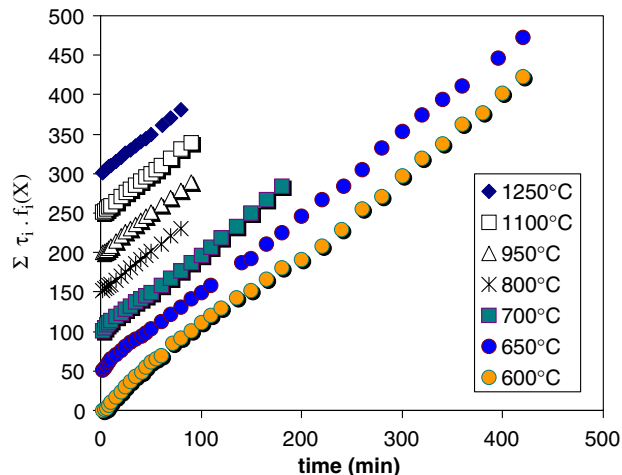


Fig. 6. Two-step controlling plots for changes of the fractional weight-loss functions against time for $n_A = 0.3$ at different temperatures. Note that 50 units with respect to the lower temperature vertical shifting is made to separate the graphs.

around $D_{PD} = 2 \times 10^{-5}$, $D_{ID} = 1 \times 10^{-6}$ m²/s, and $k_s = 4 \times 10^{-5}$ m/s.

These data are evaluated from the following double-stage controlling mechanisms:

- (a) either of the following two processes
 - (i) pore inter-diffusion of the gases, or
 - (ii) internal diffusion outwards and inwards the active reaction sites within the sample.
- (b) CA of the gaseous reaction species on the surface of flat graphite flakes.

The external boundary layer mass transfer effect is assumed insignificant. The relative activation energies obtained at different stages approve this assumption. Effective coefficients for the pore or internal diffusion (D_{PD} and D_{ID}) and the rate constant of the CA reaction (k_s) can be evaluated from the following total conversion time equations:

Table IV. Kinetic Parameters Evaluated for Various Andreason Distribution Coefficients at Different Temperatures by Applying the Experimental Results into the Mathematical Model Developed in this Research. (a) $600^\circ \leq T \leq 800^\circ\text{C}$ and (b) $800 \leq T < 1250^\circ\text{C}$

(a)	n_A	$T(^\circ\text{C})$	b	τ_{ID}	τ_{CA}	τ_{PD}/τ_{CA}	D_{PD} (cm ² /min)	k_s (cm/min)
	0.3	800	1.92	407.96	127.31	3.20	9.7060247	0.05529
	0.3	700	1.67	1101.89	263.66	4.18	2.0652071	0.02727
	0.3	650	1.47	2767.70	355.36	7.79	0.8333667	0.01977
	0.3	600	1.27	13178.65	0	∞	0.2284841	0.52618
	0.5	800	1.92	523.79	130.89	4.00	7.7616268	0.05522
	0.5	700	1.67	2428.1	299.25	8.11	1.7390969	0.02509
	0.5	650	1.47	7568.66	400.88	18.88	0.6012559	0.02018
	0.5	600	1.27	18980.16	60.98	311.25	0.1994386	0.57592
	0.7	800	1.92	477.29	135.8	3.51	8.4861390	0.05302
	0.7	700	1.67	1963.81	280.73	6.99	2.1422362	0.02664
(b)	n_A	$T(^\circ\text{C})$	b	τ_{ID}	τ_{CA}	τ_{PD}/τ_{CA}	D_{PD} (cm ² /min)	k_s (cm/min)
	0.3	1250	2	230.17	19.38	11.88	21.924904	0.52618
	0.3	1100	2	295.50	29.56	10.00	17.336380	0.34443
	0.3	950	1.98	329.10	34.32	9.59	13.247474	0.19223
	0.5	1250	2	309.11	17.1	18.08	17.921251	0.57592
	0.5	1100	2	350.03	27.49	12.73	14.267462	0.32296
	0.5	950	1.98	404.41	45.54	8.88	11.110941	0.17541
	0.7	1250	2	366.87	18.47	19.86	15.155862	0.53518
	0.7	1100	2	364.94	26.48	13.78	13.684550	0.33528
	0.7	950	1.98	420.46	47.07	8.933	10.686809	0.16971

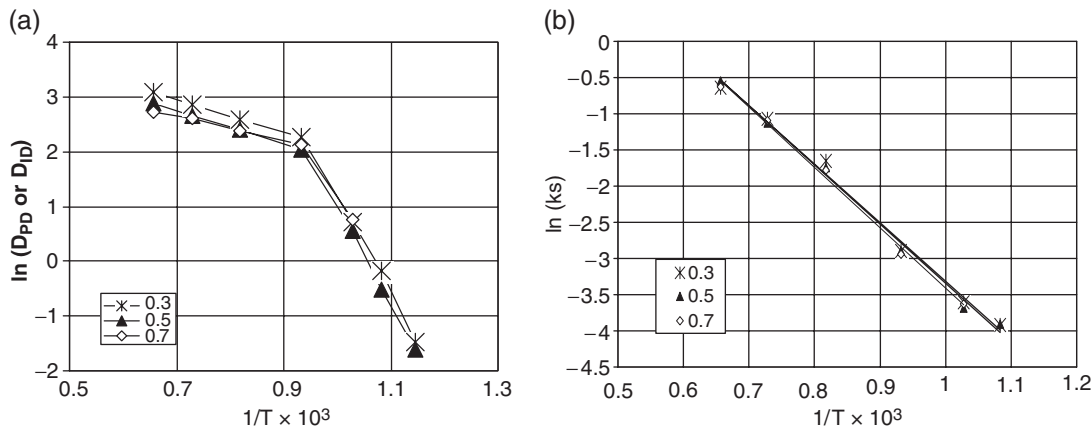


Fig. 7. Arrhenius plot of (a) pore or internal diffusion and (b) chemical adsorption.

$$\tau_{PD} = (\rho_p R^2)/(4bC_{O_2} D_{PD}) \tag{18}$$

$$\tau_{ID} = (\rho_p R^2)/(4bC_{O_2} D_{ID}), \tag{19}$$

$$\tau_{CA} = (\rho_{Gr} L)/(bC_{O_2} k_s) \tag{20}$$

C_{O_2} is the oxygen concentration around the external surface of the probes, b is the stoichiometric coefficient of the oxidation reaction, D_{PD} is the pore inter-diffusion of the gas, D_{ID} is the mean internal diffusion coefficient of the gases and k_s is the effective rate constant of the chemisorption reaction. The apparent molar density of the graphite in the MgO-C probe (ρ_p) is proportional to the mean density of the cylindrical probe

$$\rho_p = \rho_{MgO-C} \times \%G/12 \tag{21}$$

where $\%G$ is the weight percent of graphite flakes in the MgO-C brick. Arrhenius law plots of the diffusion and the chemisorption processes are demonstrated in Fig. 7. The activation energies (Q_{ij}) and the frequency factors (A_{ij}) of different stages are determined from the respective slopes and intercepts of the $\ln D_{ij}$ or $\ln k_s$ versus $1/T$ graphs. The subscript ij stands for CA at temperature range 600–1250°C, internal diffusion (ID) at temperature range 600–800°C, and pore diffusion (PD) at temperature range 800–1250°C. The activation energies and the frequency factors thus obtained are illustrated in Table V.

Different activation energies are recognized for different conditions. A moderate value of ~68 kJ/mol is observed for CA of the gases on the surface of the graphite flakes. This value is the same for all temperatures considered in our investigation. High-temperature diffusion process shows relatively small (~22 kJ/mol) activation energies associated with the pore inter-diffusion of the oxidizing gas toward the interior of the porosity holes present in the refractory brick. Because of the large graphite combustion at these temperatures, the pores are generally large and open-ended. The inter-diffusion of the gases is therefore convenient. At lower temperatures, however, the holes are generally closed and the species must diffuse through the solid sub-

Table V. Activation Energy and Frequency Factor of Different Kinetic Steps Evaluated for Three Andraesen Distribution Coefficients Given

n_A	0.7	0.5	0.3
$Q_{CA}^{600^{\circ}-1250^{\circ}C}$ (kJ/mol)	69.29	67.98	67.18
$Q_{ID}^{600^{\circ}-800^{\circ}C}$ (kJ/mol)	119.49	143.06	144.37
$Q_{PD}^{800^{\circ}-1250^{\circ}C}$ (kJ/mol)	18.11	25.08	24.54
$A_{CA}^{600^{\circ}-1250^{\circ}C}$ (cm/min)	137.9	125.3	117.7
$A_{ID}^{600^{\circ}-800^{\circ}C}$ (cm ² /min)	5.57×10^6	7.54×10^7	1.1×10^8
$A_{PD}^{800^{\circ}-1250^{\circ}C}$ (cm ² /min)	64.55	129.57	150.25

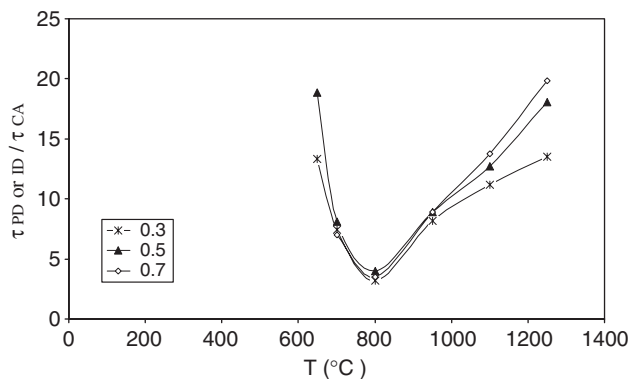


Fig. 8. Effect of temperature on τ_{PD} or ID/τ_{CA} ratio for different Andraesen distribution coefficients.

stances covering the flakes. This process has relatively large mean activation energy of ~140 kJ/mol. Relatively low diffusion coefficients accompanied with the high activation energies below 800°C indicate the soot blockage of the MgO pores and the difficulty for local transfer of the substances (Fig. 3).

Ignoring the effect of the chemical reaction,[‡] previous authors have determined film transfer and pore diffusion activation energies of around 47¹⁵ and 48 kJ/mol^{13,15} at 1000–1200°C, respectively. The former is much larger than the values generally accepted for film transfer.^{27,28} The latter is much greater than the activation energy of 20.9 kJ/mol reported for 800–1200°C by Ghosh *et al.*¹⁴ The reported value of Ghosh *et al.*¹⁴ is around the same activation energy as obtained in this research.

Variation of the controlling step is illustrated in Fig. 8 by plotting the ratio of the total conversion time for the CA to the total conversion time for diffusion (pore or solid) against temperature and Andraesen number. Around 800°C, a minimum appears in all graphs plotted in Fig. 8. This is another indication for change of the mechanism at this temperature. The nature of the diffusion process occurring below this temperature is totally different from what happens at the higher temperatures. This can easily be conferred from the huge Arrhenius plot slope change around 800°C (Fig. 7(a)).

Careful observations indicated the formation of soot and its blocking of the holes channeling to the graphite flakes in the MgO-C bricks during oxidation (Fig. 3). The quantity of the soot considerably increases below 800°C. A comparison of the XRD count numbers for graphite peaks versus soot peaks proves clearly this effect (see Figs. 5 and 9).

Figure 10 shows the average density and porosity of the probes measured after heating at 240° and 600°C versus And-

[‡]Chemical adsorption of gas on the surface of the graphite flakes according to our treatment.

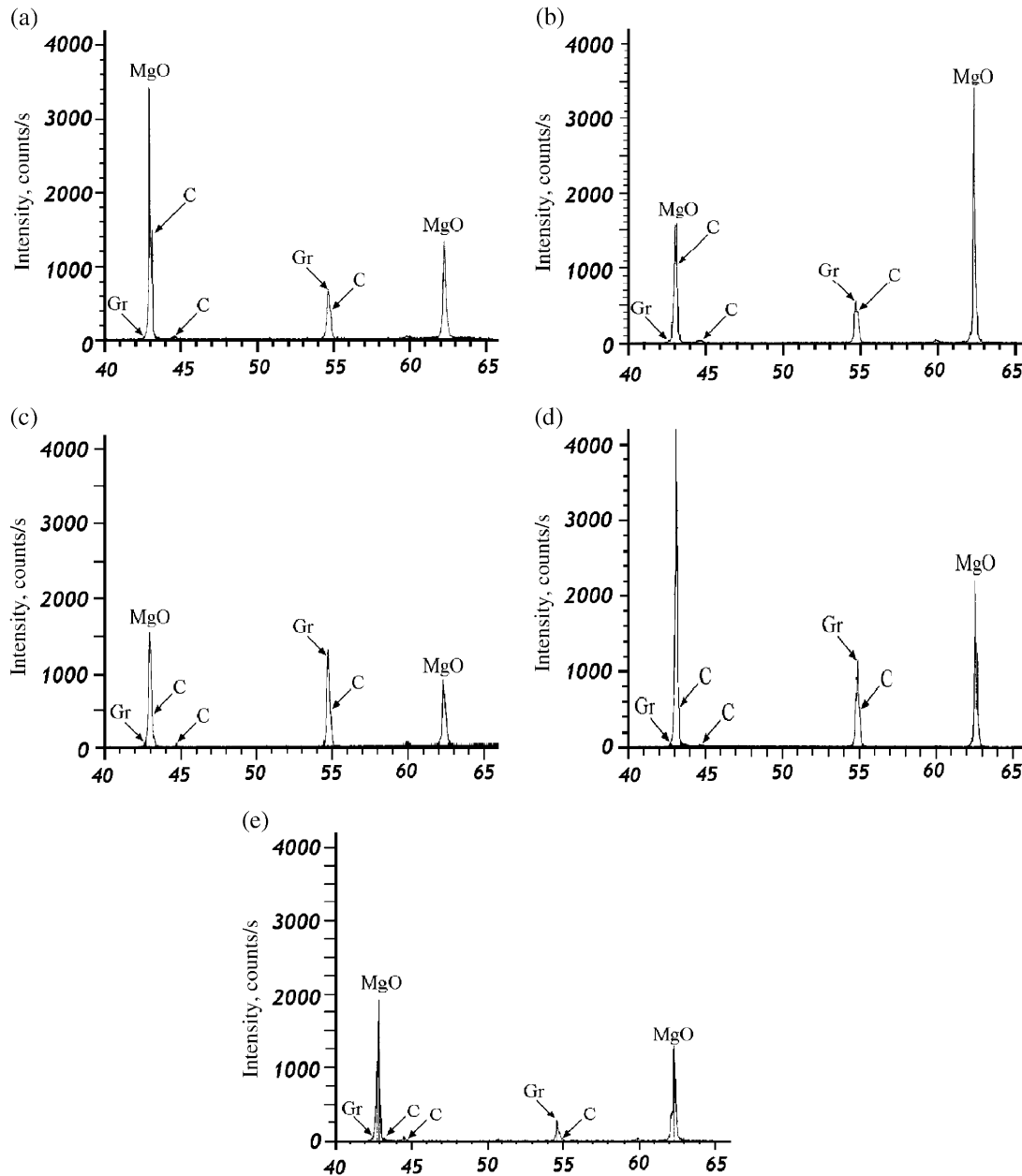


Fig. 9. X-ray diffraction peaks of graphite and amorphous carbon in the MgO-C samples produced after oxidation with air at (a) 600°C, (b) 650°C, (c) 700°C, (d) 750°C, and (e) 1100°C. Notice that the count numbers of peaks attributed to soot becomes too small at 1100°C.

reased distribution coefficient. It is seen that increasing the Andreason number increases the density and decreases the porosity of the MgO-C samples. At small Andreason numbers when the proportion of the MgO fines is high, the MgO particles can fit in the spaces between graphite plates, which can stay far apart from each other. Such a wide distribution can produce higher porosity after sample oxidation. At high Andreason numbers, tight packing of graphite flakes in the interstices between the medium and coarse oxide particles results in extremely efficient packing and lower porosity caused after burn out of the graphite flakes.¹⁰ Because of these changes, one would expect that the total conversion times associated with the pore diffusion step must increase with increasing of the Andreason number. This is simply the case with the graphs plotted (Fig. 8), which show higher τ_{PD} or t_D/τ_{CA} ratios at temperatures greater than 800°C. At the lower temperatures, a different diffusion mechanism prevails and the effect of the Andreason number is not as significant as at the higher temperatures (see Fig. 8).

At high n -values, fewer fine particles are present. With a fixed percentage of graphite in the probes, the graphite flakes would tightly pack the materials together. The interstices between the

medium and the coarse oxide grains will be filled with the graphite flakes. This leads to a quite condensed body. The change in the density and porosity of the samples are not significant when Andreason number enhances from $n = 0.5$ to 0.7. This is indicated by previous authors.¹⁰ The changes in the τ_{PD} or t_D/τ_{CA} ratio shown in Fig. 8 are small with these Andreason numbers even at high temperatures ($T > 800^\circ\text{C}$).

Inter-diffusion of the gases within the pores consists of concomitant inward O_2 versus outward CO/CO_2 transfer through the decarburized layer. This process occurs by molecular, Knudsen or surface diffusion. The share of each stage depends on the pore's structure and volume of the oxidized layer. The effective diffusion coefficient is defined as²⁹

$$D_{PD} = D_{\text{O}_2\text{CO or O}_2-\text{CO}_2} \cdot \epsilon \gamma \quad (22)$$

$D_{\text{O}_2\text{CO or O}_2-\text{CO}_2}$ is the molecular inter-diffusivity of oxygen and CO/CO_2 gas mixture, ϵ is the porosity content of the oxidized layer and γ is the shape factor of the pores. The porosity content of the oxidized layer is a function of the initial porosity of the probe and volume of the oxidized graphite. As the initial

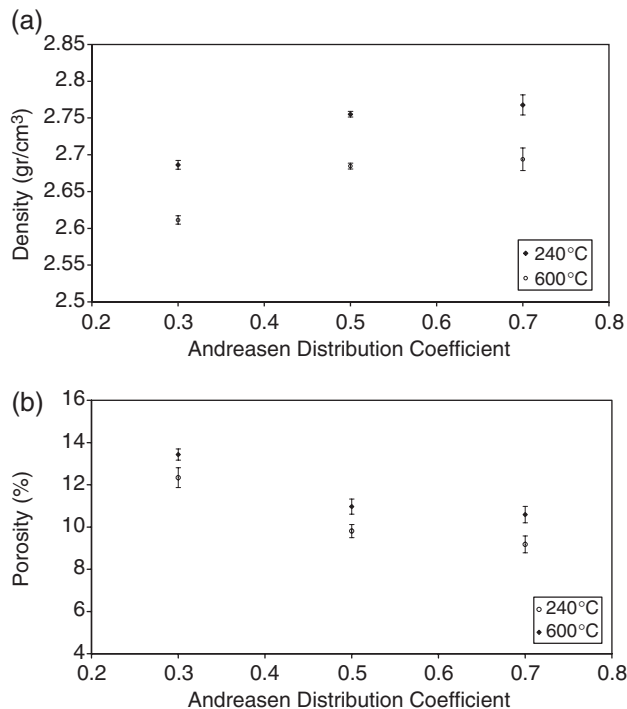


Fig. 10. Effect of Andraesen distribution coefficient on (a) density and (b) porosity of the MgO-C probe.

porosity of the body increases, the diffusion of gases will be easier and consequently more weight loss is expected.

Since determination of γ is not experimentally easy, it is approximated from Eq. (22). The total porosity content of the oxidized layer is calculated based on the initial porosity and the initial graphite content of the sample. Substituting the values of ϵ and D_{PD} into Eq. (22), one can obtain the amount of the inter-diffusion coefficient times the shape factor γ .

The theoretical value of the inter-diffusion coefficient is obtained from the Chapman-Enskog equation.³⁰ Substituting in Eq. (22), the values of γ are obtained (Table VI). A comparison of the experimental values with the theoretical ones can be made to assess the accuracy of the treatment. Table VI shows that a shape factor of about $\gamma = 0.5$ satisfies the correlations at 1100°C. This is roughly consistent with the tortuosity values specified by previous researchers.³¹

V. Practical Applications

Resin-bonded MgO-C bricks provide valuable properties essential to many high-technology applications. They are used in pyrometallurgical practices like iron and steel manufacturing processes for lining of ladles, oxygen converters, and arc furnaces. These materials serve at different temperatures from ambient to 800°C and higher. An example is a VOD vessel in which the temperature significantly changes with time and location. At the face opposite the hot face of the refractory bricks, for example, the temperature is relatively low. In the nose region, the temperature rises during tapping as high as liquid steel temperature. It reduces to a relatively low temperature during charging,

Table VI. Evaluation of Tortuosity Coefficient at 1100°C Based on D_{PD} Values Obtained in this Research

n_A	D_{PD} (cm ² /min)	ϵ	γ
0.3	17.33	0.13	0.49
0.5	14.27	0.10	0.41
0.7	13.68	0.09	0.56

D_{O_2-CO} is estimated to be 270 cm²/min at 1100°C.²⁷

repairing, and idling of the vessel. Temperature fluctuations are observed in all areas of a vessel depending on the frequency of the heats usually taken.

Air oxidation occurs in all industrial vessels working at different temperatures. A comprehensive understanding of MgO-C behavior under practical conditions helps to optimize refractory performance especially under severe carbon burnout with oxygen. Prediction of graphite oxidation rate is an essential piece of information required for oxidation prevention and refractory life determination. Grain size distribution shown by Andraesen number and temperature distribution are two important factors that can be used to restrict the rate of graphite oxidation.

This study shows that the effect of pore diffusion and internal gas transfer is much greater than that of the CA at temperatures studied here (600°–1250°C). Prevention from oxidation can, hence, be accomplished with increasing of all possible barriers against inter-diffusion of gases within the porous decarburized region as well as solid-phase gas transfer inside the MgO grains encircling the graphite flakes.

Lengthening of the lifetime of the MgO-C bricks according to the soot formation mechanism opens a new frontier for another class of MgO-C bricks especially designed for low-temperature metal processing vessels. Purposeful addition of soot to the compacted MgO-C refractory grains may be of help in lengthening the lifetime of the refractory MgO-C bricks.

VI. Conclusions

Shrinking core and progressive conversion models are combined together to devise a computer software that predicts the most probable rate controlling steps governing the MgO-C oxidation reaction. The rate controlling steps are determined by utilization of the best-fit method comparing the experimental results with the mathematical data. Results indicate that in the range of 600°–1250°C, mixed controlling regimes govern the rate of the process. Dual step mechanisms with different structural details are found to prevail at different 600°–800°C and 800°–1250°C temperature ranges. Soot formation appears to have a substantial effect on the prevailing mechanism.

Below 800°C, the CA of the gases plus the internal diffusion within the local solid layers surrounding the graphite flakes are the two ruling processes. Above 800°C, the CA of the gases at the active reaction sites and the inter-diffusion of the gases throughout the porous decarburized area of the cylindrical probes govern the rate of the graphite oxidation.

The experimental data obtained in this research are used to determine the total conversion times and the activation energies of all three processes. A higher value of ~ 140 kJ/mol is related to the local diffusion into the solid layers surrounding the graphite phase. A lower value of 22 kJ/mol is attributed to the pore inter-diffusion of the gases toward the active reaction sites. CA of the gases to the surface of the flat graphite flakes has a moderate activation energy of around 68 kJ/mol.

Observations indicate increasing of the density and decreasing of the porosity of the samples with the Andraesen distribution coefficient. The weight-loss data show that the rate of oxidation is reversely influenced by the Andraesen number. The coefficients for pore inter-diffusion, local solid phase diffusion and chemisorption reaction are found to be respectively around 2×10^{-5} , 1×10^{-6} m²/s, and 4×10^{-5} m/s. A tortuosity factor of around 0.5 is obtained for MgO-C bricks initially containing 14.3% graphite and 4.8% phenolic resin oxidized at 1100°C with air.

References

1. Yamaguchi, S. Zhang, and S. Hashimoto, "Behaviour of Antioxidants Added to Carbon-Containing Refractories"; pp. 341–8. *Unitect Proceedings 95*, Japan, 1995.
2. S. Banerjee, "Recent Developments in Steel-making Refractories"; pp. 1033–41. *Unitect' 01 Proceedings 91*, Mexico, 2001.

- ³S. K. Sadrnezhad, *Heat and Motion in Materials*. Foreign Ministry Press, Tehran, Iran, 1999, (ISBN 964-330-526-X).
- ⁴A. Watanabe, H. Takahashi, and F. Nakatani, "Mechanism of Dense Magnesia Layer Formation Near the Surface of Magnesia–Carbon Brick," *J. Am. Ceram. Soc.*, **69** [9] c-213–4 (1986).
- ⁵B. Baker and B. Brezny, "Dense Zone Formation in Magnesia–Graphite Refractories"; pp. 168–72. *Unitec Proceedings* 91, Germany, 1990.
- ⁶A. Yamaguchi, "Control of Oxidation–Reduction in MgO–C Refractories," *Taikabutsu Overseas*, **4** [1] 32–7 (1984).
- ⁷M. Rigaud, C. Richmond, and P. Bombard, "Oxidation Kinetics of Graphite in Basic Refractory Composites"; pp. 266. *Unitec Proceedings* 91, Germany, 1991.
- ⁸V. L. Lou, T. E. Mitchell, and A. H. Heuer, "Graphical Displays of the Thermodynamics of High-Temperature Gas–Solid Reactions and their Application to Oxidation of Metals and Evaporation of Oxides," *J. Am. Ceram. Soc.*, **68** [2] 49–58 (1985).
- ⁹A. Yamaguchi, "Effects of Oxygen and Nitrogen Partial Pressure on Stability of Metal, Carbide, Nitride and Oxide in Carbon-Containing Refractories," *Taikabutsu Overseas*, **7** [1] 4–13 (1987).
- ¹⁰N. C. Lubaba, B. Rand, and N. H. Brett, "Compaction Studies of MgO-Flake Graphite Mixtures Relevant to the Fabrication of Composite Refractory Materials," *Br. Ceram. Trans.*, **87**, 158–63 (1988).
- ¹¹M. Subbanna, P. C. Kapur, and Pradip, "Role of Powder Size, Packing, Solid Loading and Dispersion in Colloidal Processing of Ceramics," *Ceram. Int.*, **28**, 401–5 (2002).
- ¹²M. Suzuki, H. Sato, M. Hasegawa, and M. Hirota, "Effect of Size Distribution on Tapping Properties of Fine Powders," *Powder Technol.*, **118**, 53–7 (2001).
- ¹³X. Li, M. Rigaud, and S. Palco, "Oxidation Kinetics of Graphite Phase in Magnesia–Carbon Refractories," *J. Am. Ceram. Soc.*, **78** [4] 965–71 (1995).
- ¹⁴N. K. Ghosh, D. N. Ghosh, and K. P. Jagannathan, "Oxidation Mechanism of MgO–C in Air at Various Temperature," *Br. Ceram. Trans.*, **99** [3] 124–8 (2000).
- ¹⁵M. A. Faghihi-Sani and A. Yamaguchi, "Oxidation Kinetics of MgO–C Refractory Bricks," *Ceram. Int.*, **28**, 835–9 (2002).
- ¹⁶B. Hashemi, Z. Moghimi, Z. A. Nemat, and S. K. Sadrnezhad, "Solid–Gas Reactions in MgO–C Refractories"; pp. 581–9 in *4th ISARIM-Symposium on Refractories*, Eds. M. Rigaud and C. Allaire MET Society, Hamilton, Canada, 2004.
- ¹⁷B. Hashemi, Z. A. Nemat, and S. K. Sadrnezhad, "Oxidation Mechanisms in MgO–C Refractories," *China's Refractories*, **13** [2] 13–8 (2004).
- ¹⁸S. K. Sadrnezhad, A. Gharavi, and A. Namazi, "Software for Kinetic Process Simulation," *IJE Trans. A: Basics*, **16** [1] 61–72 (2003).
- ¹⁹N. Mazet and B. Spinner, "Modeling of Gas–Solid Reactions 2. Porous Solids," *Int. Chem. Eng.*, **32** [2] 271–84 (1992).
- ²⁰E. Achenbach, "Three-Dimensional and Time-Dependent Simulation of a Planar Solid Oxide Fuel Cell Stack," *J. Power Sources*, **49**, 333–48 (1994).
- ²¹A. Y. Watson and P. A. Valberg, "Carbon Black and Soot: Two Different Substances," *American Industrial Hygiene Association Journal*, **62** [2] 218–2 (2001).
- ²²A. Mayer, "Definition, Measurement and Filtration of Ultrafine Solid Particles Emitted by Diesel Engines," pp. 1–8, TTM, ATW-EMPA-Symposium, 19 April, 2002.
- ²³S. Campanari and P. Iora, "Definition and Sensitivity Analysis of a Finite Volume SOFC Model for a Tubular Cell Geometry," *J. Power Sources*, **132**, 113–26 (2004).
- ²⁴C. G. Aneziris, D. Borzov, and J. Ulbricht, "Magnesia–Carbon Bricks: A High-Duty Refractory Material," *Interceram Refractories Manual*, 22–5 (2003).
- ²⁵B. Rand, A. S. Ahmed, and V. P. S. Ramos, "The Role of Carbon in Refractories," *Tehran Int. Conf. Refractories*, 40–55 (2004).
- ²⁶V. Wiesche, A. Gardziella, R. Solozabal, and J. Suren, "Synthetic Resins as Carbon Forming Agents for Various Refractories: Carbon Yields, Analytical Methods, Structures and Emissions"; pp. 260–4. *Unitec Proceedings* 91, Germany, 1991.
- ²⁷O. Levenspiel, *Chemical Reaction Engineering*. John Wiley, New York, 1972, (BN 0-471-53016-6).
- ²⁸K. J. Laidler, *Chemical Kinetics*. McGraw-Hill, New York, 1965.
- ²⁹R. W. Missen and C. A. Mims, *Introduction to Chemical Reaction Engineering and Kinetics*, pp. 224–36. John Wiley and Sons Inc, New York, 1999.
- ³⁰G. H. Geiger and D. R. Poirier, *Transport Phenomena in Metallurgy*. Addison-Wesley Publication Company, Reading, MA, 1973.
- ³¹J. Szekely, J. W. Evans, and H. Y. Sohn, *Gas-Solid Reactions*. Academic Press, New York, 1976. □